


Experimentally Finding Dense Subgraphs Using a Time-Bin Encoded Gaussian Boson Sampling Device

S. Sempere-Llagostera¹, R. B. Patel^{1,2}, I. A. Walmsley¹ and W. S. Kolthammer¹

¹*Department of Physics, Imperial College London,
Prince Consort Road, London SW7 2AZ, United Kingdom*

²*Clarendon Laboratory, University of Oxford, Parks Road, Oxford OX1 3PU, United Kingdom*

 (Received 21 June 2022; revised 26 August 2022; accepted 29 August 2022; published 30 September 2022)

Gaussian boson sampling is a quantum computing concept based on drawing samples from a multimode nonclassical Gaussian state using photon-number resolving detectors. It was initially posed as a near-term approach to achieve quantum advantage, and several applications have been proposed since, including the calculation of graph features. For the first time, we use a time-bin encoded interferometer to implement Gaussian boson sampling experimentally and extract samples to enhance the search for dense subgraphs in a graph. Our results indicate an improvement over classical methods for subgraphs of sizes three and four in a graph containing ten nodes. In addition, we numerically explore the role of imperfections in the optical circuit and on the performance of the algorithm.

DOI: [10.1103/PhysRevX.12.031045](https://doi.org/10.1103/PhysRevX.12.031045)

Subject Areas: Optics, Photonics, Quantum Information

I. INTRODUCTION

Quantum computing promises to modify the current computational paradigm [1,2] by providing a substantial speedup in the computation of specific tasks that are currently intractable. Two key milestones achieved so far are (i) theoretically developing algorithms that show a quantum speedup compared to the classical counterpart [3] and (ii) experimentally implementing protocols that surpass the capabilities of traditional computers [4,5]. Meeting these two at a common ground to show a quantum advantage in practical applications is a compelling next step. Progress toward a fault-tolerant universal quantum computer brings us closer to this goal, yet it is possible that a shortcut is provided by simpler, limited-purpose computers, perhaps without error correction [6].

In the optical domain, Gaussian boson sampling (GBS) has emerged as a potential candidate in this regard [7,8]. GBS involves injecting a multimode nonclassical Gaussian state into an interferometer and measuring the number of photons at each output. The classical procedure to simulate this sampling problem is not efficiently computable on a classical computer [7,9]. Specifically, it requires the computation of a mathematical function called the Hafnian, which constitutes a $\#P$ -hard problem. Thus far, GBS has found applications both as a subroutine in the bigger

quantum computer picture as a resource state generator [10,11] and as a stand-alone device that can be used, for instance, to calculate vibronic spectra of molecules or graph features [12–14]. Concerning the two key aforementioned milestones, a quantum advantage has been achieved by means of a GBS experiment [5,15], but no practical application has been demonstrated yet. However, in a recent paper, Arrazola *et al.* [16] showed promising results employing a fully reconfigurable small-scale eight-mode GBS device for the calculation of molecular vibronic spectra and graph similarity. A particular application of GBS is the enhancement of algorithms to search for dense subgraphs. This concept is integral to a broad class of clustering problems with varied applications [13], for example, analyzing social networks and discovering communities residing within them [17,18].

A technical challenge of optical interferometers at the core of GBS is to scale them up to a large number of modes, while achieving low loss and reconfigurability. Traditionally, the information carried by an optical state is encoded in its polarization or spatial modes, implying the need for extensive hardware requirements when employing a few dozens of photons. As shown by Reck *et al.* [19], the number of beam splitters needed to implement an arbitrary $m \times m$ unitary matrix is $m(m-1)/2$. In the context of quantum information processing and GBS, these have been implemented in various forms, for instance, using bulk optics [20] and in integrated platforms [21–23]. Other nonuniversal approaches have been achieved using bulk optics [24] and fiber architectures [25,26], the largest to date being a bulk optics interferometer with 144 input-output modes [15]. A recent proposal [27] suggested using the temporal modes to encode the

Published by the American Physical Society under the terms of the Creative Commons Attribution 4.0 International license. Further distribution of this work must maintain attribution to the author(s) and the published article's title, journal citation, and DOI.

information as a means to scale up for boson sampling experiments. This scheme is attractive for its scalability and reconfigurability [20], while exhibiting comparable losses [28,29] to the other reconfigurable platforms [23]. Furthermore, in this approach, the number of components is fixed regardless of the size of the implemented unitary. In principle, arbitrary scale can be achieved with minor hardware modifications. Alternative nonuniversal time-bin interferometers have been proposed to achieve quantum supremacy via high-dimensional GBS [30].

In this work, we (i) implement a 20-mode time-bin interferometer to conduct a GBS experiment and (ii) experimentally show how such a GBS device can enhance the search for dense subgraphs. In particular, we demonstrate this for subgraphs of sizes three and four in a graph of ten nodes. This constitutes the first experimental realization of GBS in a time-bin encoded manner and the first application of a GBS machine to improve the search of dense subgraphs.

This paper is structured as follows. First, we introduce the main concepts of Gaussian boson sampling, the time-bin interferometer, and the use of GBS to search for dense subgraphs in a graph. Then, we describe the experimental work, which combines these three elements, and show the results obtained. Finally, we perform numerical calculations to study the role of imperfections for the particular application of finding dense subgraphs.

II. THEORY

A. Gaussian boson sampling

Figure 1(a) illustrates the concept of Gaussian boson sampling. We consider an m -mode system with separable Gaussian state inputs that undergoes a transformation characterized by the transfer matrix Λ , followed by single-photon detection. The input states $|\xi_i\rangle$ can be chosen from the spectrum of Gaussian states, for instance, vacuum, squeezed vacuum, or coherent states, among others. The interferometer only consists of linear optical elements and loss, which are Gaussian transformations [31]. Therefore, the state at the

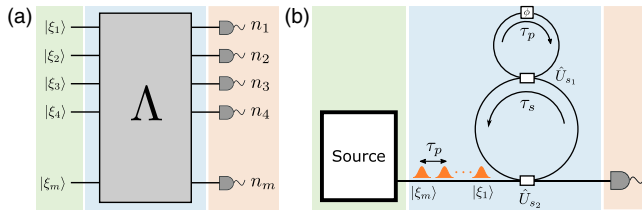


FIG. 1. (a) General GBS picture, where we have an m -mode Gaussian state going into an interferometer described by the transfer matrix Λ and then detected using single-photon detectors. (b) Time-bin encoded architecture to implement GBS experiments. The modes are defined by temporal bins, and the interferometer is implemented by optical loops. One light source generates the multimode input state, which is detected at the output by one single-photon detector.

output is also Gaussian and can be completely described by a $2m \times 2m$ covariance matrix Σ and a displacement vector α . With no displacement, i.e., $\alpha = 0$, the probability to measure a certain output pattern $\mathbf{n} = (n_1, n_2, n_3, \dots, n_m)$ is given by [7]

$$P(\mathbf{n}) = \frac{P(0)}{\prod_i n_i!} \text{Haf}(A_{\mathbf{n}}), \quad (1)$$

where $P(0)$ is the probability of not detecting any photons at the output and Haf is the Hafnian function. The Hafnian of a matrix is computed as

$$\text{Haf}(A) = \sum_{M \in \sigma(n)} \prod_{(i,j) \in M} A_{i,j}, \quad (2)$$

where $\sigma(n)$ indicates the set of perfect matching permutations of n objects (see Appendix A for details). The matrix A can be derived from the covariance matrix as

$$A = X(I - Q^{-1}), \quad (3)$$

where

$$X = \begin{pmatrix} 0 & I \\ I & 0 \end{pmatrix}, \quad (4a)$$

$$Q = \Sigma + I/2, \quad (4b)$$

where I is the identity matrix of appropriate dimension. The submatrix $A_{\mathbf{n}}$ is obtained by selecting n_i times the i th and $(i+m)$ th rows and columns of A . Consequently, $A_{\mathbf{n}}$ is a square matrix that grows with the total number of detected photons N , with $N = \sum_i n_i$. The matrix A can be decomposed into a block matrix of the form

$$A = \begin{pmatrix} B & C \\ C^T & B^* \end{pmatrix}, \quad (5)$$

where B is an $m \times m$ symmetric matrix and C is an $m \times m$ Hermitian matrix.

In the particular case of having a pure Gaussian state with no displacement at the output, A can be further reduced to $A = B \oplus B^*$, i.e., $C = 0$, and the probability to measure a detection pattern \mathbf{n} becomes

$$P(\mathbf{n}) = \frac{P(0)}{\prod_i n_i!} |\text{Haf}(B_{\mathbf{n}})|^2, \quad (6)$$

where the submatrix $B_{\mathbf{n}}$ is obtained by selecting n_i times the i th rows and columns. Note that in this case, the matrix $B_{\mathbf{n}}$ will be of size $N \times N$ and, due to the nature of the Hafnian, N needs to be even. This agrees well with the fact that if there is no loss present in the system, which would add mixedness to the state, photons will always come in

pairs from the squeezed vacuum states and, therefore, detecting an odd number of photons will not be possible.

B. Time-bin interferometer

Here we introduce the concept of a time-bin interferometer [27], motivate its usage, and explain how its structure relates to the resulting mode transformation. A time-bin implementation of GBS is illustrated in Fig. 1(b). We can distinguish three main parts that are interfaced by a common spatial mode: the light source, the interferometer, and the detection.

The light source generates a train of pulses with separation τ_p , which defines the time-bin modes and contains the input states $|\xi_i\rangle$. The fact that we only need a single source to run the whole experiment, as opposed to many sources [5,21] or demultiplexing techniques [22,24], poses a significant simplification in terms of experimental resources. In addition, enlarging the size of the problem is straightforward, as it solely requires letting more pulses into the interferometer.

A remarkably simple design for a time-bin interferometer, which we implement below, consists of a single optical loop with a time-independent coupling to the input-output field. The round-trip time of the loop is matched to the separation of consecutive pulses. An optical circuit model of this scenario is shown in Fig. 2(a). Each pulsed mode in the input, denoted by a numbered line, interacts sequentially with a pulsed mode in the loop, denoted by the line \mathcal{A} . The coupling between the loop and the input-output mode is described by B_i , corresponding to a general two-mode beam-splitting operation.

The transfer matrix elements for an ideal single-loop interferometer are

$$\Lambda_{i,j} = \begin{cases} 0 & \text{if } j < i \\ \cos(\theta) & \text{if } j = i \\ -\sin^2(\theta)[\cos(\theta)]^{(j-i-1)} & \text{if } j > i, \end{cases} \quad (7)$$

where i and j label the input and output modes, respectively, and the amplitude transmittivity of the beam splitter

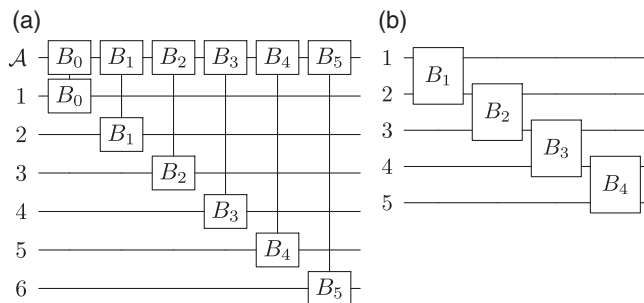


FIG. 2. (a) Optical circuit of a pass through the single loop, for input modes 1–6, loop mode \mathcal{A} , and beam splitter operations B_i . (b) Effective circuit for input modes 1–5 where modes \mathcal{A} and 6 are initially vacuum and B_0 and B_5 are fully reflective.

is given by $\cos(\theta)$. The case $j > i$ is understood intuitively as consisting of $j - i$ round-trips in the loop. The corresponding element $\Lambda_{i,j}$, therefore, contains the product of two reflection amplitudes, from coupling in and out of the loop, with $j - i - 1$ transmission amplitudes. Note that the magnitudes of the matrix elements decay exponentially with the mode separation, which is a consequence of the time-independent beam splitter. Furthermore, optical loss arising in the beam splitting or loop propagation, which has not been included here for simplicity, further increases this decay.

While the simple static loop device implements a limited class of interferometers specified by the beam splitter angle θ , devices with additional loops and time-dependent beam splitters are able to implement arbitrary transfer matrices [27,28]. We now extend the single-loop model to this general case. First, consider one pass by a loop with time-dependent beam splittings, as depicted in Fig. 2(a), for which the initial and final beam splitters are fully reflective, effectively swapping the mode states. For an example of input states on modes 1–5, where modes \mathcal{A} and 6 are initialized with vacuum states, the output states are returned on modes 2–6. In Fig. 2(b), the auxiliary vacuum modes are disregarded, and we show the effective circuit of the resulting operation, where passing through the loop is seen to enact a series of beam-splitting operations between consecutive modes.

An arbitrary interferometer can be implemented by concatenating these programmable single-loop operations. In particular, any interferometer with m input modes can be achieved with $m - 1$ single-loop operations, according to the decomposition by Reck *et al.* [19]. A convenient approach for this is shown in Fig. 1(b), where two loops are arranged to appear as a snowman. The larger lower loop is connected to the input-output field by a time-dependent switch s_2 , and this loop is sufficiently long to store the entire train of pulses. For each round-trip in this storage loop, the pulse train interacts with the smaller upper loop, which processes the modes by the single-loop operation, mediated by the time-dependent beam splitter s_1 . Alternate loop configurations may be used to implement arbitrary interferometers using other decompositions [32,33], which might offer practical improvements in mitigating nonuniform loss incurred across different input-output pairs [29]. Lastly, we note that universality may still be achieved for limited beam-splitting values [34,35], at the cost of additional round-trips and corresponding optical loss.

Finally, we have the detection system. This presents another substantial improvement of this architecture over other platforms. Because of the temporal encoding of the information, we can potentially reduce the required number of detectors to one, compared to the spatial encoding depicted in Fig. 1(a) in which we need m . This feature can become very relevant when scaling up to bigger interferometers. The main practical consideration is the

reset time of the detectors being larger than the time-bin spacing, which could skew the output statistics.

C. Finding dense subgraphs using a GBS device

Here we review the connection between GBS outcome statistics and the identification of highly connected subgraphs, as introduced by Ref. [13]. To start, we note that any graph may be described by its adjacency matrix Δ , where the matrix element Δ_{ij} gives a weight associated with the edge connecting node i to node j . For the case of an undirected graph, Δ is a symmetric matrix; i.e., $\Delta_{ij} = \Delta_{ji}$. In Eq. (5), we see that a pure Gaussian state with zero displacement may be described by the symmetric matrix \mathbf{B} . This establishes a correspondence between the quantum state and an undirected graph, in terms of its adjacency matrix. Moreover, Eq. (6) shows that the probability of any particular GBS outcome from this state is related to the Hafnian of a subgraph of \mathbf{B} .

The connectivity of a graph can be expressed by its density, defined as

$$d = 2 \frac{\sum \Delta_{ij}}{n(n-1)}, \quad (8)$$

where the sum runs over all edges of the graph and $n = \dim(\Delta)$ is the number of nodes in the graph. For an unweighted graph, for which $\Delta_{ij} \in \{0, 1\}$, the density corresponds to the ratio of $\sum \Delta_{ij}$ to its maximum possible value. A key step by Arrazola and Bromley [13] is to show that $\text{Haf}(\Delta)$, which is equal to the number of perfect matchings in the graph, is a useful indicator of the graph density, and therefore, the outcome statistics from GBS can be used to identify dense subgraphs. In particular, they show that search algorithms with access to GBS outcomes outperform those based on uniform random searches. In our work, this concept is applied to the broader case of weighted graphs. In general, the GBS-enhanced search constitutes an example of the advantage provided by proportional sampling over random search in specific optimization problems, as shown in Ref. [36]. For a further discussion of these graph concepts, see Appendix A.

The recipe for employing a GBS device for this purpose is given in Ref. [14] as follows.

- (1) Decompose \mathbf{B} , which describes the graph we want to study, into a unitary matrix \mathbf{U} and a vector λ using the Takagi-Autonne decomposition. These will correspond to the linear interferometer and squeezing parameters at each of the input modes, respectively.
- (2) Compile \mathbf{U} into the appropriate beam splitter and phase-shifting operations of the linear interferometer. Program the interferometer accordingly.
- (3) Rescale the squeezing parameters $r_i = \tanh^{-1}(c\lambda_i)$ according to the constant $c > 0$ such that $\langle n \rangle = \sum_{i=1}^n (c\lambda_i)^2 / (1 - (c\lambda_i)^2)$. In the case of an n -node subgraph, this can be used to maximize the

probability of obtaining an n -fold coincidence at the output. Note that this rescaling does not change the n -fold relative probability distribution. Program the squeezers accordingly.

After following this procedure the GBS device will generate a sample outcome \mathbf{n} , with probability

$$P(\mathbf{n}) \propto \frac{c^N}{\prod_i n_i!} |\text{Haf}(\mathbf{B}_{\mathbf{n}})|^2, \quad (9)$$

where $N = \sum_i n_i$ is the total number of detected photons. We can then feed these samples into a classical algorithm to find dense subgraphs in a graph, for instance, as shown in Ref. [13].

An unavoidable imperfection in optical systems is loss. In experiments involving single-photon states, as is the case of standard boson sampling, uniform loss in the interferometer can be neglected by postselecting on the same number of photons as we had at the input. So, in this scenario, loss will ultimately affect our detection rates solely, but the probability distribution at the output for some n -fold detection will remain unaffected. The situation is rather different when employing other types of input states, for instance, single-mode squeezed vacuum (SMSV). In the case of GBS, it is easy to see that if we have loss in the system, we will not have a pure state anymore, and, therefore, $\mathbf{C} \neq 0$ and we would be sampling from a different distribution. The impact on how this imperfection affects our ability to use GBS to find dense subgraphs in a graph is studied in Sec. V.

III. EXPERIMENT

Our implementation of time-bin encoded GBS is depicted in Fig. 3. A mode-locked Ti:sapphire laser produces 100-fs pulses at a repetition rate of 80 MHz. A Pockels cell-based pulse picker acts as a shutter to create isolated pulse sequences that correspond to individual trials. The off time between trials ensures the initialization of the loop to vacuum. We use a half-wave plate (HWP) and polarizing beam splitter (PBS) combination to control the energy of the pulses sent to the setup. A pair of angle-tuned bandpass filters shape the spectrum of the incoming pump pulses appropriately to obtain degenerate and factorable emission via spontaneous parametric down-conversion (SPDC) from a type-II periodically poled potassium titanyl phosphate (PPKTP) waveguide [37–39]. The two orthogonally polarized fields of the approximate two-mode squeezed vacuum (TMSV) state generated in the nonlinear process are split using a Wollaston prism and coupled into polarization-maintaining (PM) single-mode fiber. Rotating the polarization of one of the fields and using a fiber-based PM 50:50 beam splitter, we recombine the two fields to generate approximate SMSV states. In this case, the two output fields do not exhibit any correlation and we can block one of them and use the other for the time-bin interferometer, preserving its purity. We send one of the outputs to the single-loop

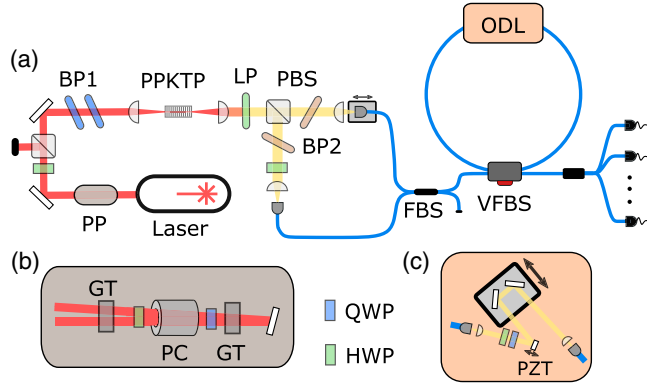


FIG. 3. (a) Main experiment setup. PP, pulse picker; BP1, bandpass filters at 775 nm; PBS, polarizing beam splitter (Wollaston prism); BP2, bandpass filters at 1550 nm; FBS, fiber beam splitter; VFBS, variable FBS; ODL, optical delay line; and LP, long pass filter. (b) Detailed schematic of the pulse-picking system, indicated as PP in (a). GT, Glan-Taylor polarizer; PC, Pockels cell; QWP, quarter-wave plate; HWP, half-wave plate. (c) Detailed schematic of the free-space optical delay in the single-loop interferometer, indicated as ODL in (a). PZT, piezoelectric actuator.

interferometer, which consists of an evanescent-field variable fiber coupler and a fiber-based loop. The length of the loop is matched to the repetition rate of the laser by using a free-space optical delay with a motorized stage, as shown in Fig. 3(c). Fine control of the loop length, which determines the phase, is achieved by using a mirror mounted on a piezoelectric actuator. Finally, the output state from the loop interferometer is analyzed using pseudo-photon-number resolving techniques via a spatially multiplexed detector.

The pulse-picking system, shown in Fig. 3(b), sets the clock-time of the experiment and uses a repetition rate of 200 kHz. The pulse configuration of the Pockels cell lets ten pulses of vacuum, ten occupied pulses, and then ten more pulses of vacuum. We are interested in those last 20 time bins, comprising a total time of 250 ns. This means that we are restricting ourselves to an effective duty cycle of 5% of the available pulses. See Appendix B for further details on this setup.

The two fields from the SPDC are coupled into single-mode fibers with an efficiency of $\eta_c = 40\%$, without including detection efficiencies. The main limitation here is the mode mismatch between the fiber and the waveguide modes, estimated to be between 60% and 70%. We can identify two main sources of loss in the interferometer: the variable fiber beam splitter (VFBS), with a throughput of $\eta_f = 90\%$ and the loss in the free-space optical delay line (ODL), with an efficiency of $\eta_o = 80\%$. Finally, the detection efficiency of the superconducting nanowire single-photon detectors is maximized by using fiber polarization controllers to be on average $\eta_d = 80\%$.

The purity of the output state, see Appendix C, is 98%. Therefore, it can be well approximated by a TMSV state, which can be expressed in the Fock basis as

$$|\text{TMSV}\rangle = \sqrt{1 - \lambda^2} \sum_{n=0}^{\infty} \lambda^n |n, n\rangle, \quad (10)$$

where $\lambda = e^{i\theta} \tanh(r)$, and r and θ are the squeezing and phase parameters, respectively. In the ideal case, interfering the idler and signal modes in a beam splitter gives a SMSV state in each output arm, namely,

$$|\text{SMSV}\rangle = \frac{1}{\sqrt{\cosh(r)}} \sum_{n=0}^{\infty} \frac{\sqrt{(2n)!}}{2^n n!} [-e^{i\theta} \tanh(r)]^n |2n\rangle, \quad (11)$$

where the squeezing in each arm is the same as that of the TMSV. The quality of the SMSV will be limited by the interference visibility between the two modes from the TMSV source. To assess this, we perform a Hong-Ou-Mandel measurement between the two fields. From a measurement of the marginal spectrum for each field, see Appendix C, we observe a slight mismatch in central wavelengths and bandwidth, leading to some distinguishability. The discrepancy in the bandwidth between the two fields originates from the group velocities in PPKTP not being symmetric with respect to that of the pump [37]. The Hong-Ou-Mandel measurement reveals a visibility of 95.3(2)%, indicating good indistinguishability. Control of the pulse energy sent to the nonlinear waveguide allows us to vary the squeezing of the SMSV states. We employ three different squeezing values in the experiment, namely, $\lambda = \{0.22, 0.31, 0.43\}$.

The single-loop interferometer achieves a sequence of beam-splitting operations between consecutive time bins, as in Fig. 2(a) without the SWAP operations. The main motivation behind the use of a single-loop structure, despite its simplicity, is the ability to apply a transformation involving a large number of modes. Figure 4(a) shows an estimation of the transfer matrix applied by the single-loop interferometer for $\phi = 0$, where ϕ is the phase of the loop. Because of the nature of the single loop, this is an upper-diagonal matrix since it is not possible to inject a photon at time bin i and detect it at output j for $i > j$. By varying the reflectivity of the VFBS, we can change the transformation matrix to some extent. In this case, this was arbitrarily set to $T = 50\%$. Likewise, Fig. 4(b) shows the modeled A matrix where, as shown, the C matrix is nonzero, denoting the mixedness of the Gaussian state. The piezoelectric actuator allows us to change ϕ and perform active phase locking; see Appendix D for details. Setting $\phi = 0$ makes both the unitary matrix U and A to be real-valued matrices.

We employ a spatially multiplexed array of eight superconducting nanowire single-photon detectors to be able to perform pseudo-photon-number resolving detection. Because of the reset time of the detectors, 60 ns, being greater than the spacing between time bins, 12.5 ns, this

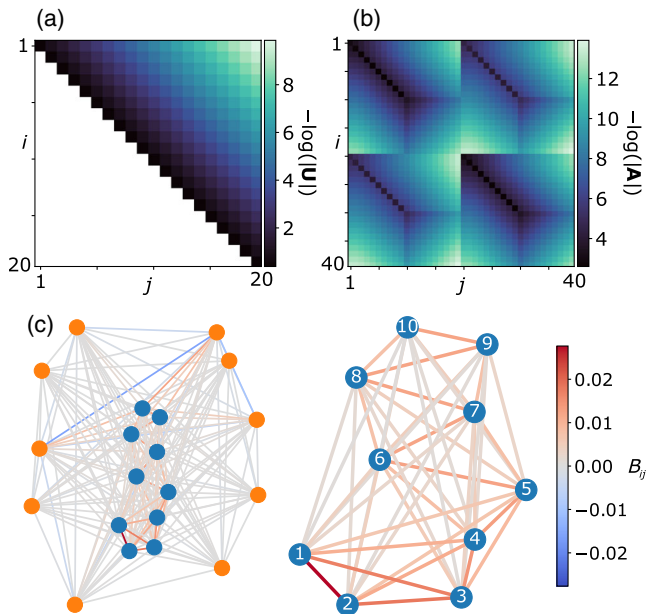


FIG. 4. (a) Transformation matrix corresponding to the single loop. (b) A of the output state. We can clearly see that the state corresponds to a nonpure Gaussian state, i.e., $C \neq 0$. (c) Left: graph defined by the symmetric part of A (top left-hand block matrix) as the adjacency matrix. The blue dots indicate the fully positive subgraph shown on the right. Right: fully positive subgraph given by nodes 1–10. The color bar indicates the weights of the edges.

type of spatially multiplexed detection is necessary to be able to resolve detections in consecutive time bins. This will impact the output detection probability. As an example, take the output state $[1, 2]$ (one detection in the first time bin, and another in the second time bin). This event will be less likely than $[1, 10]$ (second detection in the tenth time bin) since there is a greater chance of the detector being unresponsive due to the detector dead time. In our case, employing a high number of detectors allows us to neglect this effect.

IV. RESULTS

We begin by analyzing the measured photon statistics using a theoretical model of the experiment. Then, we use samples produced by the experimental device to demonstrate an enhancement in the search of dense subgraphs compared to using uniform random samples.

A. GBS output statistics

We model our experiment using the STRAWBERRYFIELDS PYTHON package [40]. For this, we use the losses described above, which are measured independently or given by the manufacturer, and assume perfect SMSV input states. The difference between the experiment and theoretical distributions can be computed using the total variation distance (TVD),

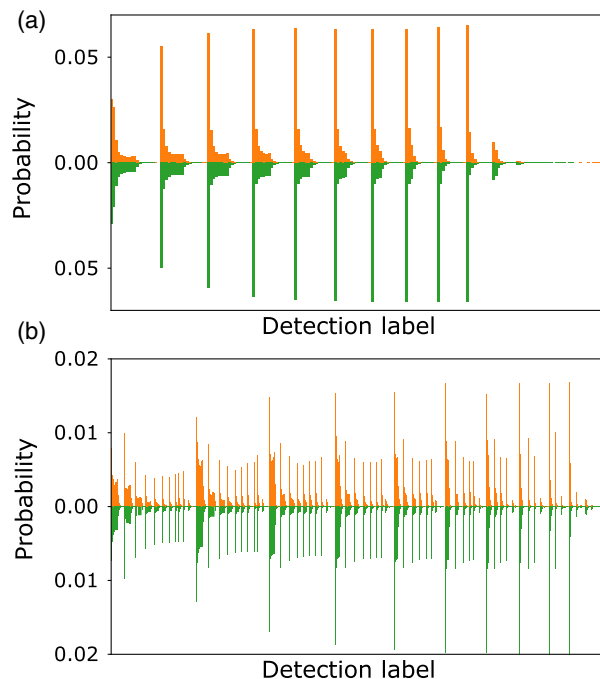


FIG. 5. Probability distribution for the twofold (a) and threefold (b) detections with an input squeezing of $\lambda = 0.31$. Green bars show the theory values and orange bars the experimental data. The x -axis detection labels are sorted in ascending order from left to right, i.e., $\{[1, 1], [1, 2], \dots, [19, 20], [20, 20]\}$ and $\{[1, 1, 1], [1, 1, 2], \dots, [19, 20, 20], [20, 20, 20]\}$, respectively.

$$D(p, q) = \frac{1}{2} \sum_i |p_i - q_i|, \quad (12)$$

where p and q are the two probability distributions we are comparing. This distance gives a measure of how close the probability distributions are, ranging from 0 to 1 for identical to completely nonoverlapping distributions, respectively. To calculate the probabilities from the model, we use Eq. (1).

We minimize the distance for the twofold detections to infer the value of the squeezing at the input. After this, for the $\lambda = 0.31$ case, we obtain a distance between the model and the experiment, $D(P_{\text{theor}}, P_{\text{expt}})$, of 0.0758(3) and 0.081(1), for the twofold and threefold coincidences, respectively, indicating the model does a good job in describing the experiment. Figure 5 shows a plot with the [Fig. 5(a)] twofold and [Fig. 5(b)] threefold probabilities obtained from the experiment and given by the model. We observe a periodic pattern depicting several exponential decays, which is characteristic of the single-loop transformation, as described by Eq. (7). In both cases, we see good agreement between the theory and the experiment. The detection rates of threefold and fourfold detections are 300 and 10 Hz, respectively. Note that the experiment rate is 200 kHz with a duty cycle of 5%, limited by the Pockels

cell. By overcoming these limitations, these rates could be increased by a factor of 20 for the same level of squeezing.

B. Finding dense subgraphs

As mentioned earlier, in a GBS experiment the graph we want to investigate is encoded in the symmetric part of \mathbf{A} , i.e., the \mathbf{B} matrix. For the purpose of identifying dense subgraphs, we require the adjacency matrix of the graph to be non-negative or nonpositive, such that the Hafnian is correlated with the density. For this, we focus on a subgraph of the graph defined by \mathbf{B} for the $\lambda = 0.31$ case that solely contains positive weights. We choose the subgraph containing nodes 1–10, which corresponds to time bins 1–10. Figure 4(c) shows both the complete graph, given by \mathbf{B} (left), and the fully positive subgraph defined by nodes 1–10 (right). Since we are interested in k -node subgraphs, we filter the obtained samples to only select nondegenerate k -fold detections. In this particular case, due to the nature of the interferometer, this has a substantial impact on the detection rates. After this postselection, we are left with 107, 312, and 1802 nondegenerate fourfold samples for $\lambda = \{0.22, 0.31, 0.43\}$ with integration times of 8, 3, and 3 h, respectively.

The use of GBS samples to identify dense subgraphs is demonstrated with a classical random search algorithm, as in Ref. [13]. In the random search algorithm, we draw n samples, each containing k nodes, calculate the density corresponding to each sample, and select the one with the maximum density. We vary the number of samples n drawn and, for each of these values, repeat the procedure 400 times and calculate the mean to remove statistical fluctuations.

Figure 6 shows the mean density obtained as a function of the number of samples drawn for subgraphs of size three [Fig. 6(a)] and size four [Fig. 6(b)]. We see that in both cases the GBS-enhanced protocols perform better than the uniform sampling case, this improvement being more prominent in the four-node subgraph case. To compare the performance of the algorithm for the different input seeds, we consider the number of samples needed, on average, to find a graph whose density is 95% of the maximum, and the mean density achieved for a given number of samples. The results are summarized in Table I and give a quantitative value of the speedup provided by the GBS device.

The ideal curve corresponds to the loss-free system. In this case, the samples are drawn directly from the distribution given by $|\text{Haf}(\mathbf{B}_n)|^2$. For the threefold case, where the Hafnian would be null due to the number of detections being odd, we use the fourfold distribution and remove one detection at random. As observed, the performance of the algorithm using these samples is the best and is considerably better than the uniform sampling case. Then, imperfections in the experimental setup mean that we do not sample anymore from \mathbf{B} [Eq. (6)] but need to use \mathbf{A} [Eq. (2)], as $\mathbf{C} \neq 0$. Crucially, we find that despite

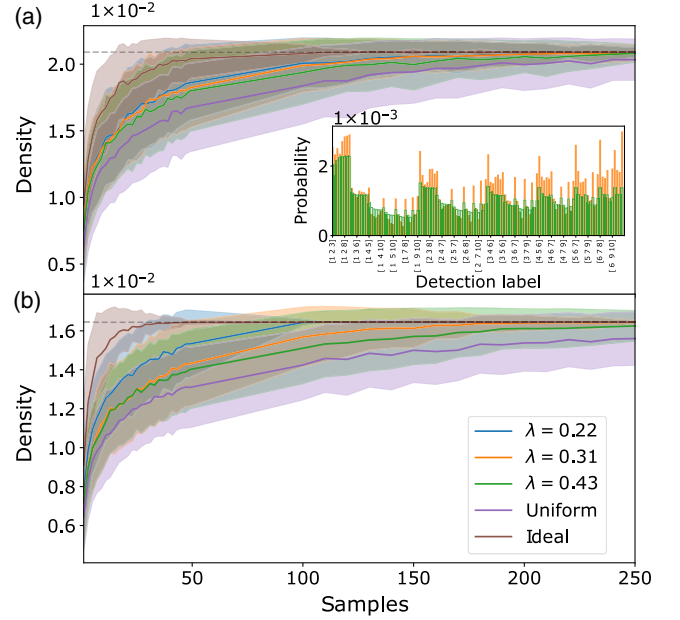


FIG. 6. (a) Mean density of the three-node subgraph as a function of the number of samples drawn. The inset shows the probability distribution for the nondegenerate output states of the experimental samples (orange filling) and the theoretical model (green edge). (b) Mean density of the four-node subgraph as a function of the number of samples drawn. The purple line indicates a uniform random search, the blue, orange, and green lines use samples obtained from the GBS experiment for different values of the squeezing as indicated in the legend, and the brown line indicates samples obtained when sampling from the distribution obtained from $|\text{Haf}(\mathbf{B}_n)|^2$. The dashed line indicates the density of the densest subgraph. The search speed decreases when increasing the squeezing. This effect is further studied in Sec. V.

significant optical loss the performance of the algorithm when using experimental samples still notably surpasses that of the uniform sampling case. Interestingly, we also notice that when increasing the squeezing the speed at

TABLE I. Subgraph search performance for different sources of random search seeds. The metrics shown are the number of samples needed to obtain a mean density of 95% and the density achieved when using 50 samples.

n	Seed	Samples at 95% density	Density for 50 samples
3	Ideal	34(1)	0.020(0)
3	$\lambda = 0.22$	92(3)	0.0186(1)
3	$\lambda = 0.31$	99(3)	0.0182(1)
3	$\lambda = 0.43$	117(4)	0.0180(2)
3	Uniform	178(5)	0.0167(2)
4	Ideal	14(1)	0.0164(0)
4	$\lambda = 0.22$	62(3)	0.0153(0)
4	$\lambda = 0.31$	98(3)	0.0143(1)
4	$\lambda = 0.43$	143(5)	0.0140(1)
4	Uniform	>260	0.0130(1)

which the curve approaches the maximum mean density decreases. Table I quantitatively illustrates this observation. This effect is studied in more detail in Sec. V.

V. LOSS AND SQUEEZING TRADE-OFF

In this section, we study how imperfections affect GBS outputs and, consequently, impact the performance of the classical algorithm to find dense subgraphs. In essence, these imperfections will change the probability distribution we are drawing our samples from, but how this modifies the performance of the algorithm for this task is not clear. Here, we focus on the most prominent imperfection in typical GBS experiments: uniform channel loss, for example, due to source-interferometer coupling or detector inefficiencies. We acknowledge that other errors such as deviations from the expected unitary or mode-dependent losses are also possible, but we leave these for future work.

To study the role of imperfections we use the following procedure.

- (1) Construct the problem graph by generating two unweighted Erdos-Renyi graphs, a small one with high edge probability and a larger one with low edge probability. Connect the nodes of the smaller graph to the nodes of the larger one at random [13].
- (2) Perform a Takagi-Autonne decomposition to obtain the squeezing and interferometer parameters that encode this graph in a GBS device. Rescale the squeezing values to change the mean photon number per mode at the output.
- (3) Add identical optical loss to each mode of GBS device model.
- (4) Using the graph and samples from the GBS model, a subgraph search is conducted as in the experiment sections above.

Here, we present results for a graph consisting of 26 nodes, where a six-node graph with edge probability 0.875 is

joined to a 20-node graph with edge probability 0.3. For the random search algorithm, we repeat the search for 1000 iterations to precisely determine the mean performance.

First, we investigate how loss modifies the normalized probability distribution for a given n -fold detection. To evaluate this, we use the TVD, introduced in Eq. (12). In other types of experiments, where we have a well-defined number of input photons, e.g., boson sampling, these probability distributions remain independent of loss. Figure 7(a) shows the TVD with respect to the lossless case and the average number of runs needed to obtain a sixfold sample, i.e., $1/p(6)$ where $p(6)$ is the probability to obtain a collision-free sixfold detection at the output, as a function of the loss for several mean photon numbers per mode, i.e., $\langle n \rangle = 1/m \sum_i \langle n_i \rangle$, where m is the number of modes. We observe that as the loss increases, the deviation from the lossless case becomes more pronounced, particularly for those cases in which the squeezing was high. In the low squeezing limit, the probability of generating instances where more photons are generated than detected, i.e., losing photons, is minimal, leading to a vanishing TVD.

Considering the number of GBS runs required for a sixfold detection event, runs/sample from hereon, we see that the choice of squeezing presents a trade-off between TVD and detection rates. We proceed to study how this compromise manifests in the search for dense subgraphs and if, at some point, allowing more runs/samples can lead to a substantial decrease in the TVD that is beneficial to this problem. An alternative to reducing the squeezing may be error mitigation [41]. This procedure involves either changing the experimental loss parameter to interpolate the measurements or performing classical postprocessing of the data. Practically, these techniques may prove challenging when studying larger systems.

The mean density obtained with n samples using a random search algorithm for several values of input loss and squeezing parameters, indicated by the corresponding

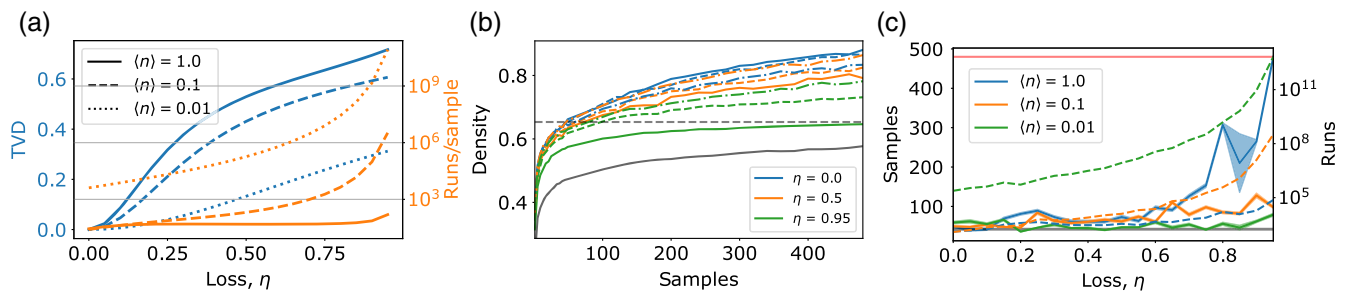


FIG. 7. (a) TVD and runs/samples as a function of the input loss for several mean photon numbers per mode at the output. (b) Density as a function of the number of samples used in the random search algorithm for several mean photon numbers indicated in the legend of (a). The different colors correspond to different input losses in the system while the black curve shows the performance of the algorithm when using uniform random samples. (c) Number of samples (solid lines) and runs (dashed lines) needed to achieve a certain mean density, defined by the black dashed line in (b), as a function of the input loss for several mean photon numbers. The shaded areas correspond to one standard deviation of the mean. The black line indicates the density achieved by the algorithm when using samples drawn directly from the adjacency matrix of the graph and the red line corresponds to uniform drawn samples. The shaded areas correspond to one standard deviation of the mean.

line colors and styles, respectively, is shown in Fig. 6(b). As observed, for a constant value of the loss, the performance of the algorithm diminishes with increasing values of squeezing, in good agreement with the experimental observations. Figure 7(c) shows the point where the mean density achieved by each of the curves in Fig. 7(b) crosses the dashed line, i.e., achieves a mean value of 75%, as a function of loss for different mean photon numbers. The speed at which the algorithm reaches a certain value for the mean density degrades as a function of the input loss for high squeezing values, but it remains unaffected when the squeezing is small. Note that in all cases, the GBS device still outperforms the uniform sampling approach indicated by the solid gray line. The dashed lines indicate the number of experimental runs needed to achieve the required number of samples needed to obtain a mean density. As shown, because the number of runs/sample increases exponentially with the mean photon number $\langle n \rangle$, in the regime we have studied, increasing the squeezing reduces the number of runs needed, in general. Because of the statistical noise of the algorithm, it is hard to extract conclusions for regimes where the variations between average photon numbers are small. Despite the success of our lossy experiment, these results indicate that for large-scale dense subgraph searches, where high squeezing values are required, further consideration of the impact of loss is likely needed. In some instances, it might even be advantageous to decrease the squeezing to reduce the TVD, despite the corresponding sacrifice in detection rates.

VI. CONCLUSIONS

We have demonstrated that measurements from a realistic GBS device can enhance the search for dense subgraphs over uniform random sampling techniques. To do so, we demonstrate GBS in a time-bin implementation with a single source of SMSV. We study up to four-photon detection events over 20 modes, showing that a single-loop interferometer can readily scale to tens of modes for this application. Then, we map the output Gaussian state to a graph and choose a subset of detection outcomes corresponding to a positive subgraph. We show that any specific outcome occurs with a probability dependent on the density of its subgraph and, therefore, demonstrate that GBS can enhance a search algorithm, e.g., random search, for the identification of dense subgraphs of a graph.

We repeat this procedure for three different squeezing parameters, observing a degradation of the algorithm's performance with increasing squeezing. To understand this, we numerically studied the role of input loss in a GBS experiment and found that the TVD with respect to the lossless case increases when using a higher squeezing. We then investigated the impact of this in the search for the dense subgraphs problem and showed that there exists a trade-off between squeezing and algorithm speed for high

values of input loss. This is in good agreement with the experimental observations.

This work constitutes the first experimental demonstration of the implementation of GBS in a time-bin encoded architecture and of how a GBS device can be employed to speed up the search of dense subgraphs. We hope this work can motivate other research groups to scale up this application to the regime where using a GBS device gives a quantum advantage. In this sense, in-depth consideration of what the consequences of imperfections are in near-term applications using GBS devices is needed.

Time-bin encoded GBS, in a fiber-based interferometer, offers many practical advantages for achieving quantum speedups in certain application areas. Our work should encourage further theoretical studies of computational problems which map onto this architecture. It will stimulate the engineering of integrated fiber-based squeezed light sources [42] as well as low-loss switching, which is essential for performing arbitrary operations on time-bin encoded states.

ACKNOWLEDGMENTS

We thank Jamie Francis-Jones for valuable input at the initial stage of this project and Guillaume Thekkadath for insightful discussions. This work was supported by Engineering and Physical Sciences Research Council via the Quantum Systems Engineering Skills Hub and the Quantum Computing and Simulation Hub (Grants No. P510257 and No. T001062).

Note added.—Recently, a closely related paper was published [43]. This work exemplifies the great potential of time-bin encoded architectures to scale up GBS experiments to a regime where they are no longer classically simulable. Our work provides a route to extend this approach to obtain a quantum advantage in a relevant application, such as the search for dense subgraphs, under realistic experimental conditions.

APPENDIX A: PERFECT MATCHINGS AND GRAPH DENSITY

To review graph concepts used in our work, let us consider an example containing six nodes, depicted in Fig. 8. Edges of this graph, shown as lines connecting the nodes, can be described by the adjacency matrix,

$$\Delta = \begin{pmatrix} 0 & 1 & 1 & 1 & 1 & 0 \\ 1 & 0 & 1 & 0 & 0 & 1 \\ 1 & 1 & 0 & 1 & 1 & 0 \\ 1 & 0 & 1 & 0 & 1 & 1 \\ 1 & 0 & 1 & 1 & 0 & 1 \\ 0 & 1 & 0 & 1 & 1 & 0 \end{pmatrix}, \quad (\text{A1})$$

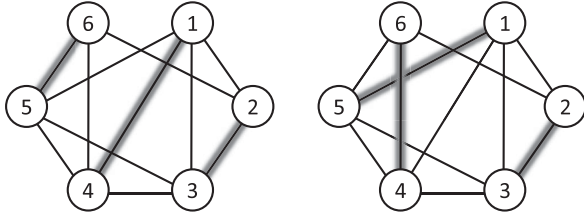


FIG. 8. An example of a six-node unweighted graph, described by the adjacency matrix in Eq. (A1). Two of the perfect matchings in the graph are shown with highlighted edges.

where the matrix element Δ_{ij} denotes the strength of the connection from node i to node j . In our work, we consider graphs that are undirected, so that $\Delta_{ji} = \Delta_{ij}$, and without loops, so that $\Delta_{ii} = 0$. Moreover, for simplicity in this example, the strength of each edge is 1 or 0, so that each pair of nodes can be thought of as either connected or unconnected. The corresponding graph is said to be unweighted.

A perfect matching in a graph is a way that the nodes are grouped into connected pairs. Two examples of perfect matching for Δ are depicted in Fig. 8. A closely related concept is the set of perfect matching permutations. This concerns all of the ways in which n objects may be grouped into $n/2$ pairs. Note that the Hafnian function $\text{Haf}(\Delta)$, defined in Eq. (2), includes a sum over the set of perfect matching permutations, for which each term consists of the selected elements of Δ multiplied together. By inspecting this definition, we see that the Hafnian of an unweighted graph is equal to the number of distinct perfect matchings it contains.

The density of a graph quantifies its connectivity. For an unweighted graph, the density is defined as the fraction of all possible connections that are present. The key insight developed in Refs. [13,44] is that the number of perfect matchings of an unweighted graph, equal to the Hafnian of its adjacent matrix, is indicative of its density. Furthermore, this relationship of the Hafnian and density is readily extended to weighted graphs.

Finally, let us consider the density of subgraphs. In our example, a four-node subgraph can be formed by removing any two nodes from the original graph. Equivalently, these subgraphs can be described as four-dimensional submatrices of Δ . The task at the center of our work is to find subgraphs with large density. For the example in Fig. 8, careful inspection finds the densest four-node subgraph contains nodes (1,3,4,5). To ease this search, one could first calculate the Hafnian of every four-dimensional submatrix of Δ as an indication of the subgraph densities. For much larger graphs, however, this direct calculation becomes impracticable.

APPENDIX B: PULSE PICKER

As shown in Fig. 3(b), as the beam enters the pulse-picking system, it first passes through a Glan-Taylor (GT)

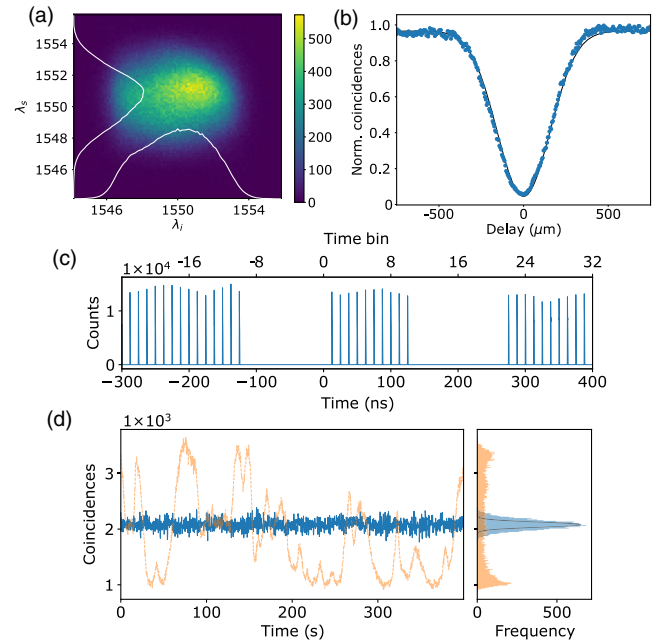


FIG. 9. (a) Joint spectral intensity of the source, with the number of counts indicated by color. (b) Hong-Ou-Mandel interference with a visibility of 95.3(2)%. The error bars, due to Poissonian counting statistics, are barely visible. (c) Timing histogram of counts at the unused output port of the FBS, demonstrating pulse picking. (d) Twofold coincidences after the interferometer for a freely running (orange) and locked (blue) loop phase. The black line in the histogram indicates fluctuations due to Poissonian statistics.

polarizer with its polarization axis aligned to the input light. A half-wave plate is then used to rotate the polarization of the beam to 45° with respect to the optic axis of the Pockels cell. The Pockels cell consists of an X-cut 20-mm ruby-dium-tantalate phosphate (RTP) crystal with an aperture of 3 mm and $V_\pi = 1$ kV. Its high-voltage driver is triggered by a digital delay generator at a repetition rate of 200 kHz. A quarter-wave plate (QWP) compensates for the natural birefringence of the RTP crystal followed by a second GT polarizer. The system is arranged in a double-pass configuration to further increase the extinction ratio, which we observe to be $1:10^5$. The overall transmission through the system is 70%. Figure 9(c) shows a histogram of the counts after the pulse picker. For the data acquisition, we gate the time tagger system to only record time tags in the $[0, 250]$ ns region, reducing the required analysis time substantially.

APPENDIX C: SOURCE CHARACTERIZATION

The joint spectral intensity of the signal and idler fields generated by SPDC, shown in Fig. 9(a), is measured with time-of-flight spectrometers that employ dispersion-compensating fibers followed by single-photon detectors. Assuming a uniform joint spectral phase, this measurement

indicates an effective mode number of 1.02. To assess the degree to which the marginal signal and idler spectra are identical, we study Hong-Ou-Mandel interference by measuring coincident photons at the output of the beam splitter (FBS) in Fig. 3 when working in the low-squeezing regime. We obtain a visibility of 95.3(2)%, defined as $(C_{\max} - C_{\min})/C_{\max}$.

APPENDIX D: PHASE LOCKING

The round-trip phase of the interferometer loop is adjusted using piezoelectric control of a mirror position. We employ a piezoelectric stack with a no-load maximum displacement of 12 μm glued to a 1/2-inch mirror. A control signal is derived from the rate at which two coincident photons are observed at the output of the interferometer. The corresponding detection events are integrated for 150 ms and used for proportional-integral-derivative control of a piezoelectric signal in the range of 0 to 7 V. Figure 4(d) compares the coincidence detection events when the loop runs freely and when it is locked.

-
- [1] M. A. Nielsen and I. L. Chuang, *Quantum Computation and Quantum Information: 10th Anniversary Edition* (Cambridge University Press, Cambridge, 2002), 10.1017/CBO9780511976667.
- [2] T. D. Ladd, F. Jelezko, R. Laflamme, Y. Nakamura, C. Monroe, and J. L. O'Brien, *Quantum Computers*, *Nature (London)* **464**, 45 (2010).
- [3] P. W. Shor, *Polynomial-Time Algorithms for Prime Factorization and Discrete Logarithms on a Quantum Computer*, *SIAM J. Comput.* **26**, 1484 (1997).
- [4] F. Arute, K. Arya, R. Babbush, D. Bacon, J. C. Bardin, R. Barends, R. Biswas, S. Boixo, F. G. Brandao, D. A. Buell *et al.*, *Quantum Supremacy Using a Programmable Superconducting Processor*, *Nature (London)* **574**, 505 (2019).
- [5] H. S. Zhong, H. Wang, Y. H. Deng, M. C. Chen, L. C. Peng, Y. H. Luo, J. Qin, D. Wu, X. Ding, Y. Hu *et al.*, *Quantum Computational Advantage Using Photons*, *Science* **370**, 1460 (2020).
- [6] V. Saggio, B. E. Asenbeck, A. Hamann, T. Strömberg, P. Schiavsky, V. Dunjko, N. Friis, N. C. Harris, M. Hochberg, D. Englund *et al.*, *Experimental Quantum Speed-Up in Reinforcement Learning Agents*, *Nature (London)* **591**, 229 (2021).
- [7] C. S. Hamilton, R. Kruse, L. Sansoni, S. Barkhofen, C. Silberhorn, and I. Jex, *Gaussian Boson Sampling*, *Phys. Rev. Lett.* **119**, 170501 (2017).
- [8] R. Kruse, C. S. Hamilton, L. Sansoni, S. Barkhofen, C. Silberhorn, and I. Jex, *Detailed Study of Gaussian Boson Sampling*, *Phys. Rev. A* **100**, 032326 (2019).
- [9] S. Aaronson and A. Arkhipov, *The Computational Complexity of Linear Optics*, in *Proceedings of the Annual ACM Symposium on Theory of Computing* (Association for Computing Machinery, New York, 2011), pp. 333–342, 10.1145/1993636.1993682.
- [10] I. Tzitrin, J. E. Bourassa, N. C. Menicucci, and K. K. Sabapathy, *Progress towards Practical Qubit Computation Using Approximate Gottesman-Kitaev-Preskill Codes*, *Phys. Rev. A* **101**, 032315 (2020).
- [11] J. Eli Bourassa, R. N. Alexander, M. Vasmer, A. Patil, I. Tzitrin, T. Matsuura, D. Su, B. Q. Baragiola, S. Guha, G. Dauphinais *et al.*, *Blueprint for a Scalable Photonic Fault-Tolerant Quantum Computer*, *Quantum* **5**, 392 (2021).
- [12] J. Huh, G. G. Guerreschi, B. Peropadre, J. R. McClean, and A. Aspuru-Guzik, *Boson Sampling for Molecular Vibronic Spectra*, *Nat. Photonics* **9**, 615 (2015).
- [13] J. M. Arrazola and T. R. Bromley, *Using Gaussian Boson Sampling to Find Dense Subgraphs*, *Phys. Rev. Lett.* **121**, 030503 (2018).
- [14] T. R. Bromley, J. M. Arrazola, S. Jahangiri, J. Izaac, N. Quesada, A. D. Gran, M. Schuld, J. Swinarton, Z. Zabaneh, and N. Killoran, *Applications of Near-Term Photonic Quantum Computers: Software and Algorithms*, *Quantum Sci. Technol.* **5**, 034010 (2020).
- [15] H. S. Zhong, Y. H. Deng, J. Qin, H. Wang, M. C. Chen, L. C. Peng, Y. H. Luo, D. Wu, S. Q. Gong, H. Su *et al.*, *Phase-Programmable Gaussian Boson Sampling Using Stimulated Squeezed Light*, *Phys. Rev. Lett.* **127**, 180502 (2021).
- [16] J. M. Arrazola, V. Bergholm, K. Brádler, T. R. Bromley, M. J. Collins, I. Dhand, A. Fumagalli, T. Gerrits, A. Goussev, L. G. Helt, J. Hundal *et al.*, *Quantum Circuits with Many Photons on a Programmable Nanophotonic Chip*, *Nature (London)* **591**, 54 (2021).
- [17] R. Kumar, P. Raghavan, S. Rajagopalan, and A. Tomkins, *Trawling the Web for Emerging Cyber-Communities*, *Comput. Netw.* **31**, 1481 (1999).
- [18] J. Leskovec, K. J. Lang, A. Dasgupta, and M. W. Mahoney, *Statistical Properties of Community Structure in Large Social and Information Networks*, in *Proceedings of the 17th International Conference on World Wide Web (WWW '08)* (Association for Computing Machinery, New York, 2008), pp. 695–704.
- [19] M. Reck, A. Zeilinger, H. J. Bernstein, and P. Bertani, *Experimental Realization of Any Discrete Unitary Operator*, *Phys. Rev. Lett.* **73**, 58 (1994).
- [20] Y. He, X. Ding, Z. E. Su, H. L. Huang, J. Qin, C. Wang, S. Unsleber, C. Chen, H. Wang, Y. M. He *et al.*, *Time-Bin-Encoded Boson Sampling with a Single-Photon Device*, *Phys. Rev. Lett.* **118**, 190501 (2017).
- [21] J. B. Spring, B. J. Metcalf, P. C. Humphreys, W. S. Kolthammer, X. M. Jin, M. Barbieri, A. Datta, N. Thomas-Peter, N. K. Langford, D. Kundys *et al.*, *Boson Sampling on a Photonic Chip*, *Science* **339**, 798 (2013).
- [22] C. Antón, J. C. Loredó, G. Coppola, H. Ollivier, N. Viggianiello, A. Harouri, N. Somaschi, A. Crespi, I. Sagnes, A. Lemaître *et al.*, *Interfacing Scalable Photonic Platforms: Solid-State Based Multi-Photon Interference in a Reconfigurable Glass Chip*, *Optica* **6**, 1471 (2019).
- [23] C. Taballione, R. van der Meer, H. J. Sniijders, P. Hooijschuur, J. P. Epping, M. de Goede, B. Kassenberg, P. Venderbosch, C. Toebes, H. van den Vlekkert *et al.*, *A Universal Fully Reconfigurable 12-Mode Quantum Photonic Processor*, *Mater. Quantum Technol.* **1**, 035002 (2021).
- [24] H. Wang, J. Qin, X. Ding, M. C. Chen, S. Chen, X. You, Y. M. He, X. Jiang, L. You, Z. Wang *et al.*, *Boson Sampling*

- with 20 Input Photons and a 60-Mode Interferometer in a 10^{14} -Dimensional Hilbert Space, *Phys. Rev. Lett.* **123**, 250503 (2019).
- [25] J. Boutari, A. Feizpour, S. Barz, C. D. Franco, M. S. Kim, W. S. Kolthammer, and I. A. Walmsley, *Large Scale Quantum Walks by Means of Optical Fiber Cavities*, *J. Opt.* **18**, 094007 (2016).
- [26] M. A. Broome, A. Fedrizzi, S. Rahimi-Keshari, J. Dove, S. Aaronson, T. C. Ralph, and A. G. White, *Photonic Boson Sampling in a Tunable Circuit*, *Science* **339**, 794 (2013).
- [27] K. R. Motes, A. Gilchrist, J. P. Dowling, and P. P. Rohde, *Scalable Boson Sampling with Time-Bin Encoding Using a Loop-Based Architecture*, *Phys. Rev. Lett.* **113**, 120501 (2014).
- [28] H. Qi, L. G. Helt, D. Su, Z. Vernon, and K. Brádler, *Linear Multiport Photonic Interferometers: Loss Analysis of Temporally-Encoded Architectures*, arXiv:1812.07015.
- [29] K. R. Motes, J. P. Dowling, A. Gilchrist, and P. P. Rohde, *Implementing BosonSampling with Time-Bin Encoding: Analysis of Loss, Mode Mismatch, and Time Jitter*, *Phys. Rev. A* **92**, 052319 (2015).
- [30] A. Deshpande, A. Mehta, T. Vincent, N. Quesada, M. Hinsche, M. Ioannou, L. Madsen, J. Lavoie, H. Qi, J. Eisert *et al.*, *Quantum Computational Advantage via High-Dimensional Gaussian Boson Sampling*, *Sci. Adv.* **8**, eabi7894 (2022).
- [31] C. Weedbrook, S. Pirandola, R. García-Patrón, N. J. Cerf, T. C. Ralph, J. H. Shapiro, and S. Lloyd, *Gaussian Quantum Information*, *Rev. Mod. Phys.* **84**, 621 (2012).
- [32] W. R. Clements, *Linear Quantum Optics: Components and Applications*, Ph.D. thesis, University of Oxford, 2018.
- [33] W. R. Clements, P. C. Humphreys, B. J. Metcalf, W. S. Kolthammer, and I. A. Walmsley, *Optimal Design for Universal Multiport Interferometers*, *Optica* **3**, 1460 (2016).
- [34] A. Bouland and S. Aaronson, *Generation of Universal Linear Optics by Any Beam Splitter*, *Phys. Rev. A* **89**, 062316 (2014).
- [35] A. Sawicki, *Universality of Beamsplitters*, *Quantum Inf. Comput.* **16**, 291 (2016).
- [36] J. M. Arrazola, T. R. Bromley, and P. Reberntrost, *Quantum Approximate Optimization with Gaussian Boson Sampling*, *Phys. Rev. A* **98**, 012322 (2018).
- [37] B. A. Bell, G. S. Thekkadath, R. Ge, X. Cai, and I. A. Walmsley, *Testing Multi-Photon Interference on a Silicon Chip*, *Opt. Express* **27**, 35646 (2019).
- [38] G. S. Thekkadath, B. A. Bell, R. B. Patel, M. S. Kim, and I. A. Walmsley, *Measuring the Joint Spectral Mode of Photon Pairs Using Intensity Interferometry*, *Phys. Rev. Lett.* **128**, 023601 (2022).
- [39] S. Sempere-Llagostera, G. S. Thekkadath, R. B. Patel, W. S. Kolthammer, and I. A. Walmsley, *Reducing $g^{(2)}(0)$ of a Parametric Down-Conversion Source via Photon-Number Resolution with Superconducting Nanowire Detectors*, *Opt. Express* **30**, 3138 (2022).
- [40] N. Killoran, J. Izaac, N. Quesada, V. Bergholm, M. Amy, and C. Weedbrook, *A Software Platform for Photonic Quantum Computing*, *Quantum* **3**, 129 (2019).
- [41] D. Su, R. Israel, K. Sharma, H. Qi, I. Dhand, and K. Brádler, *Error Mitigation on a Near-Term Quantum Photonic Device*, *Quantum* **5**, 452 (2021).
- [42] J. Lugani, R. J. A. Francis-Jones, J. Boutari, and I. A. Walmsley, *Spectrally Pure Single Photons at Telecommunications Wavelengths Using Commercial Birefringent Optical Fiber*, *Opt. Express* **28**, 5147 (2020).
- [43] L. S. Madsen, F. Laudenbach, M. F. Askarani, F. Rortais, T. Vincent, J. F. F. Bulmer, F. M. Miatto, L. Neuhaus, L. G. Helt, M. J. Collins *et al.*, *Quantum Computational Advantage with a Programmable Photonic Processor*, *Nature (London)* **606**, 75 (2022).
- [44] M. Aaghabali, S. Akbari, S. Friedland, K. Markström, and Z. Tajfirouz, *Upper Bounds on the Number of Perfect Matchings and Directed 2-Factors in Graphs with Given Number of Vertices and Edges*, *Eur. J. Combinatorics* **45**, 132 (2015).